Size Dependent Ion Diffusion in $Na_2Ti_3O_7$ and $Na_2Ti_6O_{13}$

Yuya Fukuzumi[1], Wataru Kobayashi[1234*] and Yutaka Moritomo[1234*]

[1]Graduate School of Pure and Applied Science, University of Tsukuba, Tsukuba 305-8571, Japan
[2]Faculty of Pure and Applied Science, University of Tsukuba, Tsukuba 305-8577, Japan
[3]Center for Integrated Research in Fundamental Science and Engineering (CiRfSE), University of Tsukuba, Tsukuba 305-8571, Japan
[4]Tsukuba Interdisciplinary Materials Science (TIMS), University of Tsukuba, Tsukuba 305-8571, Japan
Email: kobayashi.wataru.gf@u.tsukuba.ac.jp, moritomo.yutaka.gf@u.tsukuba.ac.jp

Abstract Titanates are promising anode materials for the lithium-ion (LIBs) and sodium-ion (SIBs) secondary batteries due to their high discharge capacity and low voltage. By means of complex impedance spectroscopy (CIS), we investigated the ion dependence of diffusion dynamics in the same host framework, *i.e.*, $Na_2Ti_3O_7$ and $Na_2Ti_6O_{13}$. In $Na_2Ti_3O_7$ with a stepped layered framework, the diffusion constant ($D_{Na} = 2.07\times10^{-10}$cm^2/s) of Na^+ is comparable to that ($D_{Li} = 2.07\times10^{-10}$cm^2/s) of Li^+ at ca. 324 K. In $Na_2Ti_6O_{13}$ with a tunneled structure, D_{Na} ($= 0.16\times10^{-10}$cm^2/s) is much lower than D_{Li} ($= 0.64\times10^{-10}$cm^2/s) at 298 K. We will discuss the size dependent ion diffusion in terms of the nanostructure of $Na_2Ti_3O_7$ and $Na_2Ti_6O_{13}$.

Keywords: secondary batteries, anode materials, titanates, ion diffusion, nanomaterial

1 Introduction

Lithium- (LIBs) and sodium-ion (SIBs) secondary batteries are significant energy storage devices due to their energy densities per weight.[1,2] Titanates are the promising anode materials for LIB because of their low toxicity, wide abundance, and low cost. Li^+ insertion occurs at low voltage between 1 - 2 V versus Li/Li^+. The most technologically important titanate for LIB is $Li_4Ti_5O_{12}$[3,4,5] with a spinel structure. In $Li_4Ti_5O_{12}$, the reduction reaction takes place via a two-phase reaction mechanism ($Li_4Ti_5O_{12}$ + 3 Li^+ + 3 e^- $\longleftrightarrow$ $Li_7Ti_4O_{12}$) at about 1.5 V versus Li/Li^+. The reaction is highly reversible as there is almost no change in volume between the two phases.[6,7]

Titanates are also the promising anode materials for SIB.[8-15] Recently, Sengutuvan *et al.*[9] found that $Na_2Ti_3O_7$ shows a high discharge capacity of 200 mAh/g and low average voltage of 0.3 V versus Na/Na^+. The voltage (= 0.3 V) is extremely low as compared with the other titanates. The discharge capacity corresponds to the following insertion reaction: $Na_2Ti_3O_7 + 2Na \rightarrow Na_4Ti_3O_7$. $Na_2Ti_3O_7$ crystal shows a monoclinic cell with space group of $P2_1/m$ ($Z = 3$)[16] and consists of zigzag $3 \times 2 \times \infty$ ribbons of the TiO_6 octahedra, in which the octahedra are linked by edges. The ribbons are two-dimensionally connected via vertices and form a stepped layered framework. On the other hand, Chiba *al.*[17] reported that $Li_2Ti_3O_7$[18] with the $Na_2Ti_3O_7$-type structure shows a high discharge capacity of 146 mAh/g and average voltage of 1.5 V versus Li/Li^+. Rousse *et al.*[10] investigated the stable structure of $Na_4Ti_3O_7$ and $Li_4Ti_3O_7$ by means of a first principle calculation. They found that the additional Na^+/Li^+ occupies the $4f$ site between the stepped layers.

Shen *et al.*[14] reported that $Na_2Ti_6O_{13}$ shows a discharge capacity of 196 mAh/g if the lower limit of the cutoff voltage is 0.0 V versus Na/Na^+. The discharge capacity corresponds to the following insertion reaction: $Na_2Ti_6O_{13} + 4Na \rightarrow Na_6Ti_6O_{13}$. $Na_2Ti_6O_{13}$ crystal shows a monoclinic cell with space group of $C2/m$ ($Z = 6$).[19] $Na_2Ti_6O_{13}$ also consists of the zigzag $3 \times 2\times \infty$ ribbons of the TiO_6 octahedra. The ribbons, however, are three-dimensionally connected via vertices and form a tunneled structure. A first principle calculation and *in situ* X-ray diffraction (XRD) suggest that the additional Na^+ are inserted into a big quasi-rectangular tunnel.[14] By means of a first principle calculation, Wang *et al.*[15] reported that Li^+ energetically prefers to stay at the small rhombic tunnels of $Na_2Ti_6O_{13}$. On the other hand, Deminko *et al,*[20,21] reported that Li^+ insertion into $Li_2Ti_3O_7$[18] with the $Na_2Ti_3O_7$-type structure causes complicated phase separation in the voltage range between 1.0 - 1.5 V versus Li/Li^+.

Thus, $Na_2Ti_3O_7$ and $Na_2Ti_6O_{13}$ are the ideal platform to investigate the ion dependence of the diffusion dynamics, because both Na^+ and Li^+ can be inserted into the same host framework.

In this paper, we reported the ion dependence of diffusion dynamics in $Na_2Ti_3O_7$ and $Na_2Ti_6O_{13}$ as investigated by complex impedance spectroscopy (CIS). We focused attention on the diffusion dynamics of the as-grown states with high crystallinity, because these compounds show complicated structural change with Li^+/Na^+ insertion and there exist few structural information except for the as-grown compound. In $Na_2Ti_3O_7$ with the stepped layered framework, the diffusion dynamics of Na^+ is quantitatively similar to that of Li^+. This indicates that the larger Na^+ does not exactly show much lower (higher) diffusion constant (activation energy) than the smaller Li^+ even in the same host framework. In $Na_2Ti_6O_{13}$ with the tunneled structure, the ion dependence of diffusion dynamics is discussed in terms of the ion-dependent diffusion channel.

2 Experiment

2.1 Sample preparation and characterization

Polycrystalline samples of $Na_2Ti_3O_7$ and $Na_2Ti_6O_{13}$ were prepared by solid state reaction. In $Na_2Ti_3O_7$, a mixture of TiO and Na_2CO_3 (= 3.00 : 1.10) was calcined at 800 °C in air for 36 hours. The product was finely ground, and calcined again at 800 °C in air for 24 h. The XRD pattern was measured using a monochromatic Cu Kα radiation. All the reflections can be indexed with the $Na_2Ti_3O_7$-type structure ($P2_1/m$; $Z = 3$). In $Na_2Ti_6O_{13}$, a mixture of TiO and Na_2CO_3 (= 6.00 : 1.05) was calcined at 800 °C in air for 20 hours. All the reflections can be indexed with the $Na_2Ti_6O_{13}$-type structure ($C2/m$; $Z = 3$).

2.2 Synchrotron-radiation X-ray diffraction

The synchrotron radiation XRD measurements were performed at BL02B2 beamline[22] at SPring-8. The powder sample was filled in a capillary and was placed on the Debye Scherrer camera at the beamline. The sample temperature was controlled by blowing cooled nitrogen gas in the temperature range of 100 K $\leq T \leq$ 300 K. The XRD patterns were recorded with an imaging plate (IP) and the exposure time was 5 min. The wavelength of the X-rays (λ = 0.50005 Å) was calibrated by the cell parameter of a standard CeO_2 powder. The accuracy of λ is restricted by energy resolution ($\Delta E/E = 2 \times 10^{-4}$) of the monochromator at BL02B2 beamline even though the lattice constant [a = 0.5411651(6) Å] of CeO2 is much higher. The Rietveld structural analyses were performed with use of the RIETAN-FP program.[23]

2.3 Complex impedance spectroscopy

To investigate the Na^+ (Li^+) diffusion dynamics in the same host framework, the CIS measurements were performed with a potentiostat (BioLogic SP-150) in a two-pole beaker-type cell against the Na (Li) metal. The measurement was performed under Ar atmosphere in an Ar filled glove box. The electrolyte is ethylene carbonate (EC)/ diethyl carbonate (DEC) containing 1M $NaClO_4$ [EC/DEC containing 1M $LiClO_4$] for Na^+ (Li^+). To obtain the cathode electrode, a mixture of a sample, ketchen black, and polyvinylidene difluoride (PVDF) (= 3 : 1 : 1 in weight ratio) was pasted on an Al foil. The active area of the electrode was about 0.7 cm^2, the frequency (f) range was from 5 mHz to 200 kHz, and the amplitude was 30 mV. The CIS were obtained at $\approx$ 2.8 V and 3.2 V for Na^+ and Li^+ respectively with the use of the as-grown sample. The temperature (T) dependence of the impedance spectra was measured in the heating run. The temperature of the beaker-type cell was controlled by a thermostat of the magnetic stirrer and actual temperature of the electrolyte was monitored with a thermocouple. We confirmed that the Nyquist curve at room temperature after the heating procedure is almost the same as the initial curve at room temperature. We found that on the whole the curves were well reproduced by the Randles equivalent circuit model (*vide infra*), which consists of the high-f resistance (R_0) of electrolyte, ionic charge-transfer resistance (R_{ct}), double layer capacitance (C_{dl}), and restricted diffusion impedance (Z_w). This clearly indicates that the curves are dominated by the Na^+ (Li^+) diffusion in bulk.

3 Results

3.1 Particle morphology

Figure 1(a) and Figure 1(b) show the scanning electron microscopy (SEM) images of $Na_2Ti_3O_7$ and $Na_2Ti_6O_{13}$, respectively. The images were obtained by a desktop-type SEM (TECHNEX Mighty-8). Insets of (a) and (b) show magnified image of the particles. The $Na_2Ti_3O_7$ particles are polyhedral, while the $Na_2Ti_6O_{13}$ particles are spherical. Figure 1(c) and Figure 1(d) show histograms of the grain radii (r) of $Na_2Ti_3O_7$ and $Na_2Ti_6O_{13}$, respectively. The average and standard deviation of r are 0.42 ± 0.23 μm and 0.36 ± 0.19 μm in $Na_2Ti_3O_7$ and $Na_2Ti_6O_{13}$, respectively.

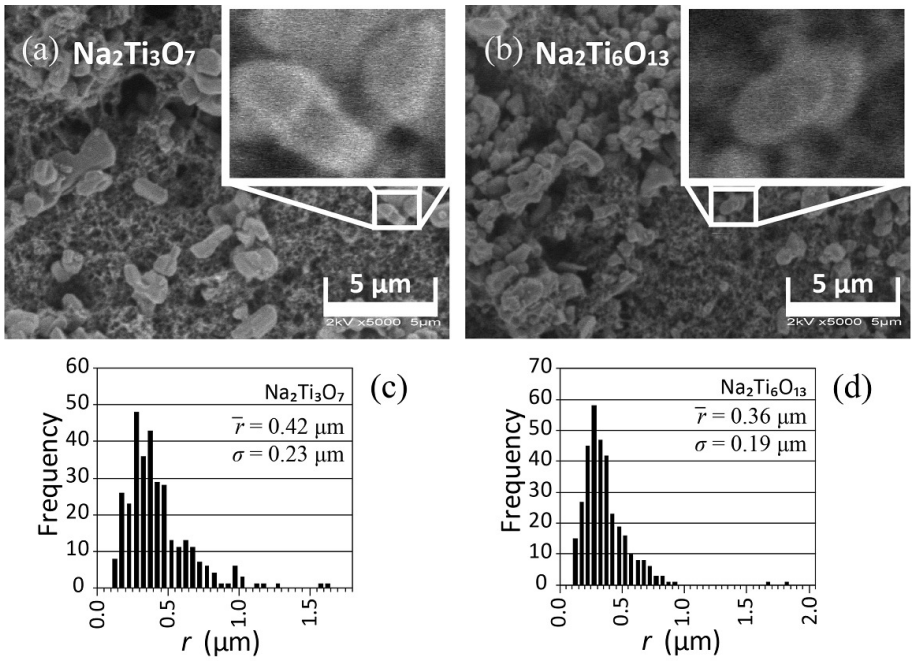

Figure 1. SEM images of (a) $Na_2Ti_3O_7$ and (b) $Na_2Ti_6O_{13}$. Insets of (a) and (b) show magnified image of the particles. Histograms of the grain radius (r) are shown for (c) $Na_2Ti_3O_7$ and (d) $Na_2Ti_6O_{13}$.

3.2 Crystal structure

Figure 2 shows the synchrotron-radiation XRD pattern of $Na_2Ti_3O_7$, together with the results of Rietveld refinement with the monoclinic model ($P2_1/m$; $Z = 3$). Overall the diffraction patterns are well reproduced with the model. The obtained structural parameters are listed in Table 1. The atomic displacement parameters (B) for Na1 and Na2 is much higher than those for the other elements and B significantly decreases with T. Thus obtained structural parameters are consistent with the literature.[10,16] Inset of Figure 2 shows the crystal structure of $Na_2Ti_3O_7$. The compound consists of $3 \times 2 \times \infty$ ribbons of the TiO_6 octahedra, which are two-dimensionally connected to form the stepped layered framework. Na^+ occupies the Na1 and Na2 sites between the layers.

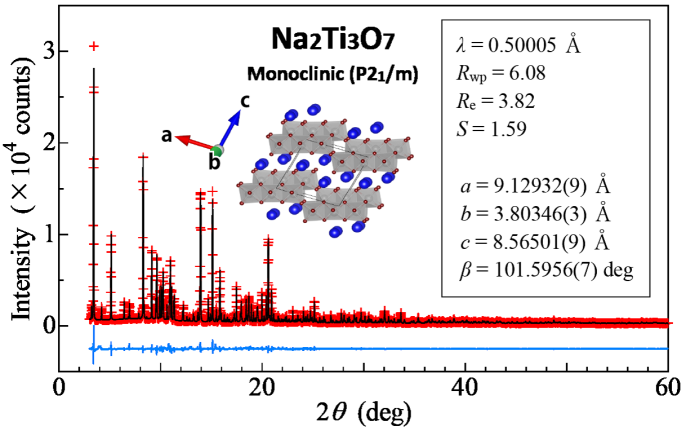

Figure 2. Rietveld refinement of the XRD pattern of $Na_2Ti_3O_7$ at 300 K. The wavelength of the X-ray was 0.50005 Å. Crosses and solid curve are the experimental data and Rietveld refinement, respectively. Lower curve is the difference between them. Small red and large blue spheres in the inset represent oxygen and sodium atoms, respectively.

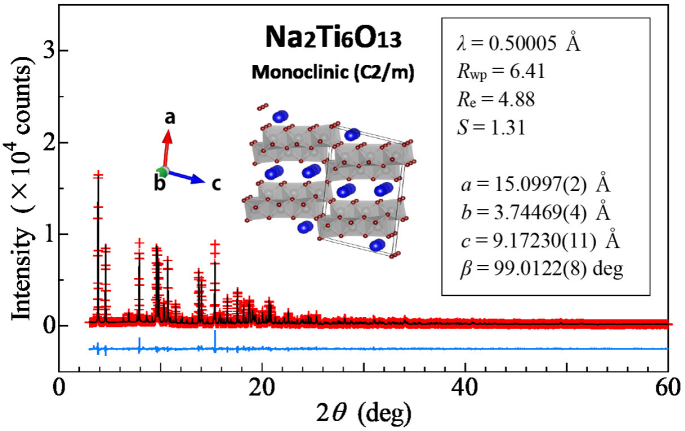

Figure 3. Rietveld refinement of the XRD pattern of $Na_2Ti_6O_{13}$ at 300 K. The wavelength of the X-ray was 0.50005 Å. Crosses and solid curve are the experimental data and Rietveld refinement, respectively. Lower curve is the difference between them. Small red and large blue spheres in the inset represent oxygen and sodium atoms, respectively.

Figure 3 shows the XRD pattern of $Na_2Ti_6O_{13}$, together with the results of Rietveld refinement with the monoclinic model ($P2_1/m$; $Z = 3$). Largely, the diffraction patterns are well reproduced with the model. The obtained structural parameters are listed in Table 2. B for Na is much higher than those for the other elements. B significantly decreases with T and the obtained structural parameters are consistent with the literature.[19] Inset of figure 3 shows the crystal structure of $Na_2Ti_6O_{13}$. The compound consists

Table 1. Atomic coordinates (x, y, z), occupancy (g) and atomic displacement parameters (B) of $Na_2Ti_3O_7$ at 300 K. The crystal structure is monoclinic ($P2_1/m$; $Z = 3$) with $a = 9.12932(9)$ Å, $b = 3.80346(3)$ Å, $c = 8.56501(9)$ Å, and $\beta = 101.5956(7)^\circ$. R_{wp}, R_e and S are 6.08%, 4.11%, and 1.59, respectively.

atom	site	g	x	y	z	B (Å^2)
Ti1	2e	1	.9852(2)	1/4	.1468(2)	0.32(1)
Ti2	2e	1	.6753(2)	1/4	.2486(2)	0.32
Ti3	2e	1	.2804(2)	1/4	.0286(2)	0.32
Na1	2e	.977(6)	.5945(4)	1/4	.6814(5)	1.69(11)
Na2	2e	.996(5)	.1546(4)	1/4	.4989(4)	1.19(10)
O1	2e	1	.1864(6)	1/4	.2191(6)	0.26(3)
O2	2e	1	.4610(6)	1/4	.1470(7)	0.26
O3	2e	1	.6508(6)	1/4	.4413(6)	0.26
O4	2e	1	.9063(6)	1/4	.3290(6)	0.26
O5	2e	1	.7525(6)	1/4	.0174(7)	0.26
O6	2e	1	.3203(6)	1/4	.8006(6)	0.26
O7	2e	1	.0436(6)	1/4	.9171(6)	0.26

of $3 \times 2 \times \infty$ ribbons of the TiO_6 octahedra, which are three-dimensionally connected to form the tunneled structure. Na^+ occupies the Na1 site between the layers.

Table 2. Atomic coordinates (x, y, z), occupancy (g) and atomic displacement parameters (B) of $Na_2Ti_6O_{13}$ at 300 K. The crystal structure is monoclinic ($C2/m$; $Z = 3$) with $a = 15.0997(2)$ Å, $b = 3.74469(4)$ Å, $c = 9.1723(1)$ Å, and $\beta = 99.0122(8)^\circ$. R_{wp}, R_e and S are 6.41%, 9.88%, and 1.31, respectively.

atom	site	g	x	y	z	B (Å^2)
Ti1	4i	1	.1143(1)	0	.0972(2)	0.31(2)
Ti2	4i	1	.1667(1)	0	.4367(2)	0.31
Ti3	4i	1	.2273(1)	0	.7710(2)	0.31
Na1	4i	0.969(6)	.4610(3)	0	.2654(4)	2.21(12)
O1	2a	1	0	0	0	0.24(4)
O2	4i	1	.2387(4)	0	.2444(6)	0.24
O3	4i	1	.0685(4)	0	.2938(6)	0.24
O4	4i	1	.2987(4)	0	.5729(7)	0.24
O5	4i	1	.1284(4)	0	.6125(6)	0.24
O6	4i	1	.3575(3)	0	.8833(5)	0.24
O7	4i	1	.1643(4)	0	.9128(6)	0.24

In Table 3, we listed the cell parameters, a, b, c, β, V of $Na_2Ti_3O_7$ and $Na_2Ti_6O_{13}$ against T. We further evaluated the coefficients of thermal expansion ($\alpha \equiv \frac{d\ln x}{dT}$; $x = a$, b, and c) and listed them in Table 3. In $Na_2Ti_3O_7$, the ribbons are two-dimensionally connected to form the stepped layered structure along c [see the inset of Figure 2]. Reflecting the layered structure of $Na_2Ti_3O_7$, α ($= 12.1(10)\times10^{-6}$ K^{-1}) along c is much higher than the other two coefficients. In $Na_2Ti_6O_{13}$, the ribbons are three-dimensionally connected to form the tunneled structure. Nevertheless, α ($= 8.5(7)\times10^{-6}$ K^{-1}) along a is slightly higher than the other two coefficients. This is probably because the connection number of the ribbons is the fewest along a in $Na_2Ti_6O_{13}$ [see the inset of Figure 3].

3.3 Diffusion constant (D_{Na}/D_{Li})

Figure 4(a) shows prototypical examples of the Nyquist plots of $Na_2Ti_3O_7$ at 297 K. Red and blue circles correspond to the Li^+ and Na^+ insertions, respectively. Let us investigate the spectrum for the

Table 3. Cell parameters, a, b, c, β, and V of $Na_2Ti_3O_7$ and $Na_2Ti_6O_{13}$ against temperature (T). The coefficients of thermal expansion ($\alpha \equiv \frac{d\ln x}{dT}$; $x = a$, b, and c) are also listed.

compound	T (K)	a (Å)	b (Å)	c (Å)	β (deg.)	V (Å^3)
$Na_2Ti_3O_7$	300	9.12932(9)	3.80346(3)	8.56501(9)	101.5956(7)	291.333(5)
	200	9.12113(9)	3.80197(3)	8.55319(9)	101.5949(8)	290.557(5)
	100	9.11511(9)	3.80111(3)	8.54433(9)	101.5952(7)	289.999(5)
	α (10^{-6}K^{-1})	7.8(7)	3.1(5)	12.1(10)	———	———
$Na_2Ti_6O_{13}$	300	15.0997(2)	3.74469(4)	9.1723(1)	99.0122(8)	512.23(1)
	200	15.0851(2)	3.74265(4)	9.1673(1)	98.9427(9)	511.28(1)
	100	15.0741(2)	3.74135(4)	9.1640(1)	98.8647(9)	510.65(1)
	α (10^{-6}K^{-1})	8.5(7)	4.5(6)	4.6(5)	———	———

Li^+ insertion. In the high-f region, the spectrum shows a semicircle and with further decrease in f, the spectrum forms a straight line with the angle of $\pi/4$ against the horizontal axis. Beyond $f = 316$ mHz, the spectrum deviates from the broken line. A similar behavior is observed in the spectra of $Na_2Ti_6O_{13}$ at 297 K [Figure 4(b)].

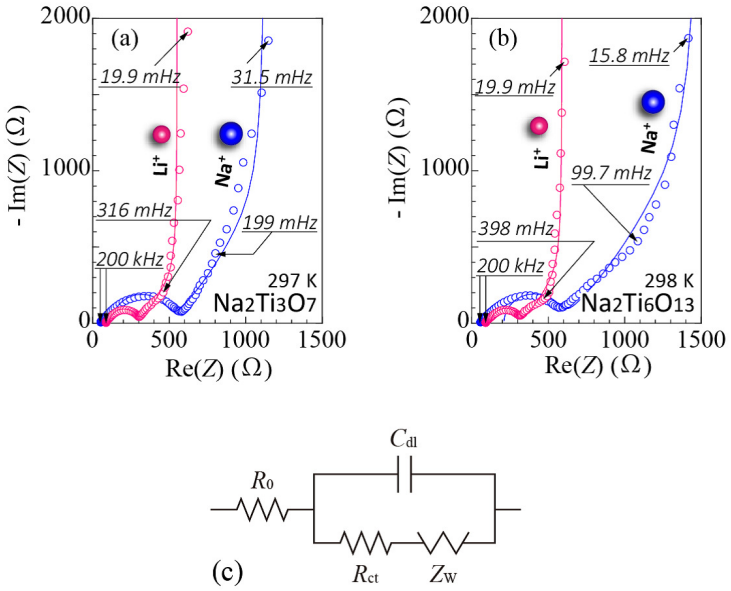

Figure 4. Nyquist plots of (a) $Na_2Ti_3O_7$ at 297 K and (b) $Na_2Ti_6O_{13}$ at 298 K. Red and blue circles correspond to the Li^+ and Na^+ insertions, respectively. Solid curves are results of the least-squares fittings with the Randles equivalent circuit model (see text). (c) Randles equivalent circuit.

We quantitatively analyzed the Nyquist plots using a Randles equivalent circuit model [Figure 4(c)], which consists of the high-f resistance (R_0) of electrolyte, ionic charge-transfer resistance (R_{ct}), double layer capacitance (C_{dl}), and restricted diffusion impedance (Z_w). Z_w is expressed as R_d Ą z_d, where R_d and z_d are the characteristic resistance and reduced diffusion impedance, respectively. z_d in the restricted spherical diffusion with radius r is expressed as

$$z_d = \frac{1}{\sqrt{u} \cdot \coth\sqrt{u} - 1}, \tag{1}$$

where u is defined by

$$u = i\frac{\omega r^2}{D}. \tag{2}$$

ω ($= 2\pi f$) and D are the angular velocity and diffusion constant, respectively. Equation (1) is derived from the Fick's second law.

We evaluated the five parameters, *i.e.*, R_0, R_{ct}, C_{dl}, R_d, and D by means of the least-squares fitting of the spectra. The solid curves in Figure 4 are the results of the least-squares fittings with the Randles equivalent circuit model. The model satisfactory reproduces the over whole behavior of the spectra. In $Na_2Ti_3O_7$ at 297 K, the obtained parameters are $R_0 = 107.0$ (126.4) Ω, $R_{ct} = 179.6$ (366.4) Ω, $C_{dl} = 4.73$ (2.08) μF, $R_d = 79.9$ (112.9) Ω,, and $D = 1.06\times$ (0.64×10^{-10}) cm^2/s for Li^+ (Na^+).

3.4 Activation energy of D_{Na}/D_{Li}

Figure 5(a) shows T-dependence of the Nyquist plots of $Na_2Ti_3O_7$ for the Li^+ insertion. The solid curves are the results of the least-squares fittings with the Randles equivalent circuit model. The diameter of the semicircle, and hence R_{ct}, is nearly independent of T. Figure 5(b) shows T-dependence of the spectra of $Na_2Ti_3O_7$ for the Na^+ insertion. The diameter of the semicircle gradually decreases with increase in T. The deformation of the semicircle, however, makes it difficult to precisely evaluate R_{ct}. Therefore, we only discuss T-dependence of D_{Li} and D_{Na}. Figure 5(c) [Figure 5(d)] shows T-dependence of the spectra of $Na_2Ti_6O_{13}$ for the Li^+ (Na^+) insertion. The T-dependence of R_{ct} is in analogy to the case of $Na_2Ti_3O_7$.

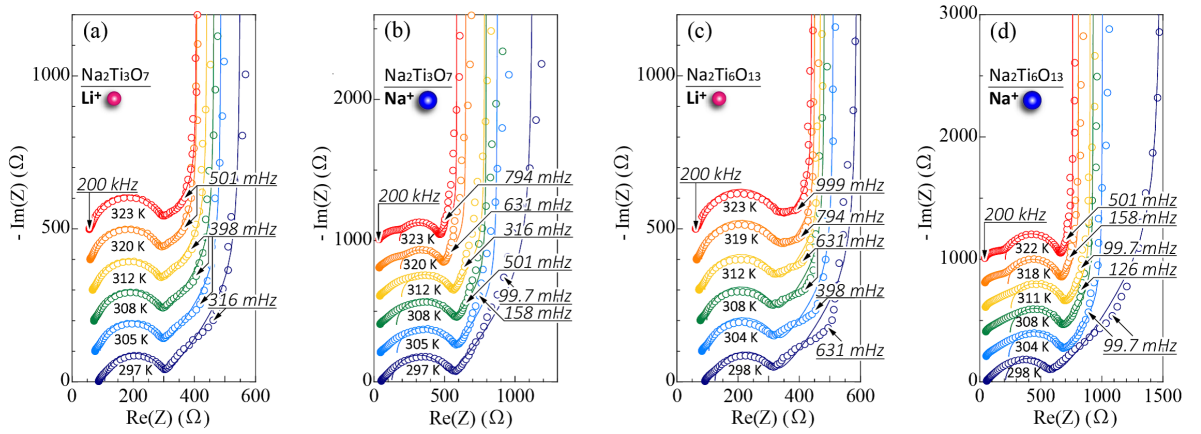

Figure 5. Nyquist plots of (a) $Na_2Ti_3O_7$ for the Li^+ insertion, (b) $Na_2Ti_3O_7$ for the Na^+ insertion, (c) $Na_2Ti_6O_{13}$ for the Li^+ insertion, and (d) $Na_2Ti_6O_{13}$ for the Na^+ insertion against temperature. Solid curves are results of the least-squares fittings with the Randles equivalent circuit model (see text).

Figure 6 shows Arrhenius plot of D_{Na} and D_{Li} and the closed circles represent D_{Na} and D_{Li} in $Na_2Ti_3O_7$. Both values linearly decrease with increase in $1/T$. As indicated by solid straight lines, we evaluated the activation energy (E_{Na}) of Na^+ and that (E_{Li}) of Li^+ and listed them in Table 4. The open circles in Figure 6 are D_{Na} and D_{Li} in $Na_2Ti_6O_{13}$. We evaluated E_{Na} and E_{Li} and listed them in Table 4.

4 Discussion

The ion dependence of diffusion dynamics in $Na_2Ti_3O_7$ is discussed with the stepped layered framework. Figure 7(a) shows the schematic structure of $Na_2Ti_3O_7$. $Na_2Ti_3O_7$ consists of zigzag $3 \times 2 \times \infty$ ribbons of the TiO_6 octahedra, in which the octahedra are linked by edges. The ribbons are two-dimensionally connected via vertices and form a stepped layered framework. The first principle calculation by Rousse *et*

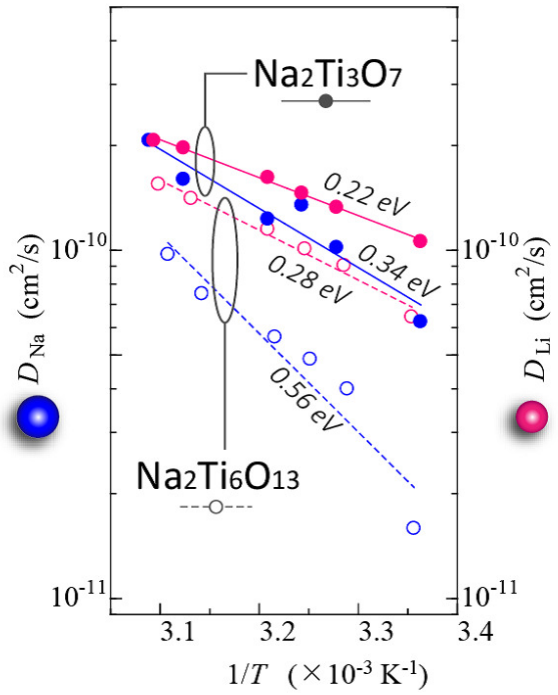

Figure 6. Arrhenius plot of D_{Na} and D_{Li}. Open and closed circles represents the data in $Na_2Ti_3O_7$ and $Na_2Ti_6O_{13}$, respectively. Solid and broken straight lines are results of least-squares fittings.

al.[10] suggests that the additional Na^+ and Li^+ occupy the same $4f$ site between the layers. The $4f$ site is sandwiched by the Na1 and Na2 sites, forming a one-dimensional diffusion channel. The ion sizes of Na^+ and Li^+ are 1.18 Å and 0.92 Å, respectively. Here, we note that the host framework is essentially unchanged during the CIS measurement, because the modulation of the Na^+/Li^+ density is only 0.002 per chemical formula at maximum. Then, the host $Na_2Ti_3O_7$ can be regarded as a rigid framework for both the Na^+ and Li^+ insertions. In Table 4, we summarized D_{Li}, D_{Na}, E_{Li}, and E_{Na} in $Na_2Ti_3O_7$. We found that D_{Li} is comparable to D_{Na}. At 323 - 324 K, D_{Li} ($= 2.07\times10^{-10}$ cm^2/s) is almost the same as D_{Na} ($= 2.07\times10^{-10}$ cm^2/s). In addition, E_{Li} ($= 0.22$ eV) is slightly lower than E_{Na} ($= 0.34$ eV).

Table 4. D_{Li}, D_{Na}, E_{Li}, and E_{Na} in $Na_2Ti_3O_7$ and $Na_2Ti_6O_{13}$.

compound	D_{Li} (10^{-11}cm^2/s)	D_{Na} (10^{-10}cm^2/s)	E_{Li} (eV)	E_{Na} (eV)
$Na_2Ti_3O_7$	1.10 (297 K)	0.62 (297 K)	0.22	0.34
	1.20 (312 K)	1.60 (312 K)		
	2.07 (323 K)	2.07 (324 K)		
$Na_2Ti_6O_{13}$	0.64 (298 K)	0.16 (298 K)	0.28	0.56
	1.06 (312 K)	0.56 (311 K)		
	1.55 (323 K)	0.97 (322 K)		

This observation looks interesting in a rigid sphere picture of Na^+/Li^+, in which a larger ion always suffers a severer steric hindrance from the host framework. However, there exists electrostatic and/or quantum-mechanical interaction between Na^+/Li^+ and the oxygen of the host framework. The smaller Li^+ tends to approach the oxygen (O^{2-}) to reduce the electrostatic energy and/or to strengthen

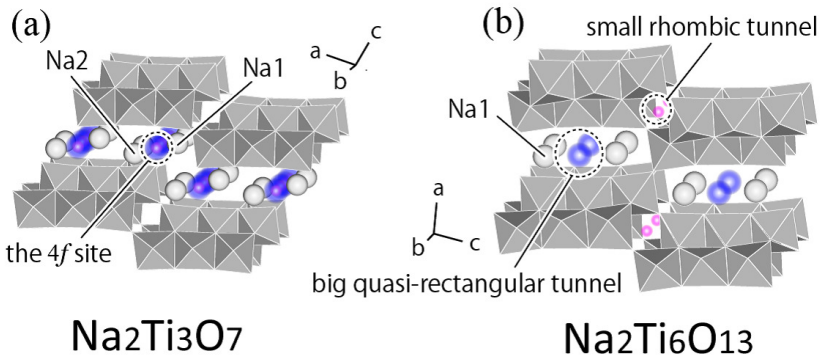

Figure 7. Schematic structure of $Na_2Ti_3O_7$ and $Na_2Ti_6O_{13}$. Large blue and small red spheres represent the additional Na^+ and Li^+, respectively.

the hybridization between the Li 2*s* and O 2*p* orbitals. Such a Li^+ - O^{2-} interaction is theoretically demonstrated by Wang *et al.* in $Na_2Ti_6O_{13}$.[15] Here, let us phenomenologically express the diffusion constants: $D_{Li} = D^0_{Li}\exp(-E_{Li}/T)$ and $D_{Na} = D^0_{Na}\exp(-E_{Na}/T)$, where D^0_{Li} (D^0_{Na}) is the diffusion constant of Li^+ (Na^+) at $T \to \infty$. D^0_{Li} and D^0_{Na} are estimated to be 5.9×10^{-8} and 3.6×10^{-6} cm^2/s, respectively. The Li^+ - O^{2-} interaction, which strongly traps Li^+ around the oxygen of the host framework, significantly suppresses D^0_{Li}. Reflecting the larger ionic size of Na^+, E_{Na} (= 0.34 eV) remains slightly higher than E_{Li} (= 0.22 eV). This means that the increase of D_{Na} with T is much steeper than that of D_{Li}. Then, D_{Li} becomes comparable to D_{Na} at higher temperature ($\approx$ 323 K).

Finally, the ion dependence of diffusion dynamics in $Na_2Ti_6O_{13}$ is discussed with the tunnel structure. Figure 7(b) shows the schematic structure of $Na_2Ti_6O_{13}$. $Na_2Ti_6O_{13}$ also consists of the zigzag $3 \times 2 \times \infty$ ribbons of the TiO_6 octahedra. The ribbons, however, are three-dimensionally connected via vertices and form a tunneled structure. The first principle calculations[14,15] suggest that the additional Na^+ and Li^+ occupy different tunnels. The larger Na^+ occupies the big quasi-rectangular tunnel, while the smaller Li^+ occupies the small rhombic tunnel. In Table 4, we summarized D_{Li}, D_{Na}, E_{Li}, and E_{Na} in $Na_2Ti_6O_{13}$ with the tunneled structure. We found that D_{Na} is much lower than D_{Li}. For example, D_{Na} ($= 0.16\times10^{-10}$ cm^2/s) is about four times lower than D_{Li} ($= 0.64\times10^{-10}$ cm^2/s) at 298 K. In addition, E_{Na} (= 0.56 eV) is twice higher than E_{Li} (= 0.28 eV). The different diffusion dynamics between Na^+ and Li^+ in the same host $Na_2Ti_6O_{13}$ framework is ascribed to the difference in the diffusion channel and the ion size. A similar ion dependence of the diffusion channel is discussed by Takachi *et al.*[24] in manganese hexacyanoferrate with a jungle-jym structure. In this system, the larger Na^+ occupies the center of the cubic nano pore, while the smaller Li^+ occupies the the face of the nano pore. They ascribed the ion dependent diffusion dynamics to the different diffusion channel.

5 Conclusions

We investigated the ion dependence of diffusion dynamics in $Na_2Ti_3O_7$ and $Na_2Ti_6O_{13}$. In $Na_2Ti_3O_7$ with the stepped layered framework, the additional Li^+ and Na^+ is reported to occupy the same 4*f* site. Nevertheless, we found that D_{Na} is comparable to D_{Li}. We ascribed the observation to the strong Li^+ - O^{2-} interaction. In $Na_2Ti_6O_{13}$ with the tunneled structure, D_{Na} is much lower than D_{Li}. In addition, E_{Na} (= 0.56 eV) is twice higher than E_{Li} (= 0.28 eV). The difference in diffusion dynamics is ascribed to the difference in the ion channel and the ion size.

Acknowledgments. This work was supported by the Nippon Sheet Glass Foundation for Materials Science and Engineering and Yazaki Memorial Foundation for Science and Technology. The synchrotron-radiation X-ray powder diffraction experiments were performed at the SPring-8 BL02B2 beamline with the approval (2015B1077 and 2013B1332) of the Japan Synchrotron Radiation Research Institute (JASRI).

References

1. M. Armand, and J. M. Trascon, "Building better batteries", *Nature*, vol **451**, pp. 652 - 657, 2008.
2. M. R. Palacin, "Recent advances in rechargeable battery materials: a chemist's perspective", *Chem. Soc. Rev.*, vo;. **38**, no. 9, pp. 2565 - 2575, 2009.
3. K. C. Kam, and M. M. Doeff, "Electrode materials for lithium ion batteries", *Mater. Matters.*, vol. **7**, no. 4, pp. 56 -62, 2012.
4. J. Liu, K. Song, P. A. Aken, J. Maier, and Y. Yu, "Self-supported $Li_4Ti_5O_{12}$-C nanotube arrays as high-rate and long-life anode materials for flexible Li-ion batteries", *Nano Lett.*, vol. **14** no. 5, pp. 2597 - 2603, 2014.
5. J. Liu, K. Tang, K. Song, P. A. Aken, Y. Yu, and J. Maier, "Tiny $Li_4Ti_5O_{12}$ nanoparticles embedded in carbon nanofibers as high-capacity and long-life anode materials for both Li-ion and Na-ion batteries", *Phys. Chem. Chem. Phys.*, vol. **15** no 48. pp. 20813 - 20818, 2013.
6. G. G. Amatucci, F. Badway, A. D. Pasquier, and T. Zheng, "An asymmetric hybrid nonaqueous energy storage cell", *J. Electrochem. Soc.*, vol. **148**, no. 8, pp. A930 - A939, 2001.
7. E. Freg, R. J. Gummow, A. de Kock, and M. M. Thackeray, "Spinel anodes for lithium A]ion batteries", *J. Electrochem. Soc.*, vol. **141**, no. 11, pp. L147 - L150, 1994.
8. M. M. Doedd, J. Cabana, and M. Shirpour, "Titanate anodes for sodium ion batteries", *J. Inorg. Organomet. Polym.*, vol. **24**, no. 1, pp. 5 - 14, 2014.
9. P. Senguttuvan, G. Rousse, V. Seznec, J. M. Tarascon, and M. R. Palacin, "$Na_2Ti_3O_7$: Lowest voltage ever reported oxide insertion electrode for sodium ion batteries", *Chem. Mater.*, vol. **23**, no. 13, pp. 4109 - 4011, 2011.
10. G. Rousse, M. E. A. Dompablo, P. Senguttuvan, A. Ponrouch, J. M. Tarascon, and M. R. Palacin, "Rationalization of Intercalation Potential and Redox Mechanism for $A_2Ti_3O_7$ (A = Li, Na)", *Chem. Mater.*, vol. **25** no. 24, pp. 4946 - 4956, 2013.
11. H. Pan, X. Lu, X. Yu, Y.-S. Hu, H. Li, X.-Q, Yang, and L. Chen, "Sodium storage and transport properties in layered $Na_2Ti_3O_7$ for room-temperature sodium-ion batteries", *Adv. Energy Mater.*, vol. **3**, no. 9, pp. 1186 - 1194, 2013.
12. A. Rudola, K. Saravanan, C. W. Mason, and P. Balaya, "$Na_2Ti_3O_7$: an intercalation based anode for sodium-ion battery applications", *J. Mater. Chem. A*, vol.**1**, no. 7, 2653 - 2662, 2013.
13. J. Xu, C. Ma, M. Balasubramanian, and Y. S. Meng, "Understanding $Na_2Ti_3O_7$ as an ultra-low voltage anode material for a Na-ion battery", *Chem. Comm.*, vol. **50**, no. 83, pp. 12564 - 12567, 2014.
14. K. Shen, and M. Wagemaker, "$Na_{2+x}Ti_6O_{13}$ as potential negative electrode material for Na-ion batteries", *Inorg. Mater.*, vol. **53**, no. 16, pp. 8250 - 8256, 2014.
15. Y. Wang, H. Zhang, X. Yao, and H. Zhao, "Theoretical understanding and prediction of lithiated sodium hexatitanates", *Appl. Mater. Interface*, vol. **5**, no. 3, pp. 1108 - 1112, 2013.
16. O. V. Yakubovich, and V. V. Kireev, "Refinement of the crystal structure of $Na_2Ti_3O_7$", *Crystallogr. Reports*, vol. **48**, no. 1, pp. 24 - 28, 2003.
17. K. Chiba, N. Kijima, Y. Takahashi, Y. Idemoto, and J. Akimoto, "Synthesis, structure, and electrochemical Li-ion intercalation properties of $Li_2Ti_3O_7$ with $Na_2Ti_3O_7$-type layered structure", *Solid State Ionics*, vol. **178**, no. 33 - 34, pp. 1725 - 1730, 2008.
18. S. Kikkawa F. Yasuda, and M. Koizumi, "Ionic conductivities of $Na_2Ti_3O_7$, $K_2Ti_4O_9$ and their related materials", *Mater. Res. Bull.*, vol. **20**, no. 10, pp. 1221 - 1227, 1985.
19. S. Anderson, and A. D. Wadsley, "The structures of $Na_2Ti_6O_{13}$ and $Rb_2Ti_6O_{13}$ and the alkali metal titanates", *Acta Cryst.*, vol. **15**, pp. 194 - 201, 1962.
20. R. Dominko, E. Baudrin, P. Umek, D. Arcon, M. Gaberscek, and J. Jamnik "Reversible lithium insertion into $Na_2Ti_6O_{13}$ structure", *Electrochem. Commun.*, vol. **174**, no. 4, pp. 673 - 677, 2007.
21. R. Dominko, L. Dupont, M. Gaberscek, J. Jamnik, and E. Baudrin, "Alkali hexatitanates $A_2Ti_6O_{13}$ (A = Na, K) as host structure for reversible lithium insertion", *J. Power Sources*, vol. **174**, no. 2, pp. 1172 - 1176, 2007.
22. E. Nishibori, M. Takata, K. Kato, M. Sakata, Y. Kubota, S. Aoyagi, Y. Kuroiwa, M. Yamakawa, and N. Ikeda, "The large Debye-Scherrer camera installed at SPring-8 BL02B2 for charge density studies", *Nuclear Inst. Methods*, vol. **467**, pp. 1045 - 1048, (2001).
23. F. Izumi, and K. Momma, "Three-Dimensional Visualization in Powder Diffraction", *Solid State Phenom.*, vol. **130**, pp. 15 - 20, 2007.
24. M. Takachi, Y. Fukuzumi, and Y. Moritomo, "Concentration dependence of Li^+/Na^+ diffusion in manganese hexacyanoferrates", *Jpn. J. Appl. Phys.*, vol. **55**, no. 6, pp. 067101, 2016.

